Surface & Coatings Technology 533 (2026) 133622

Contents lists available at ScienceDirect

Surface & Coatings Technology

journal homepage: www.elsevier.com/locate/surfcoat

Polarity-mediated mechanical reinforcement pathways in MXene-polypeptide electrospun fibers☆

Yu-Yuan Ku [a], Meng-Fang Lin [b], Tsui-Yun Chung [b], Yu-Ting Lin [b], Wen-Han Tsao [b], Jun Ohta [c], Wei-Fang Su [b], Po-Chun Chen [a,*], Yu-Ching Huang [b,d,**]

[a] Institute of Materials Science and Engineering, National Taipei University of Technology, Taipei City, Taiwan
[b] Department of Materials Engineering and Biochemical Technology R&D Center, Ming Chi University of Technology, New Taipei City, Taiwan
[c] Institute for Research Initiatives, Nara Institute of Science and Technology, 8916-5, Takayama, Ikoma, 630-0192, Nara, Japan
[d] Department of Chemical and Materials Engineering, Chang Gung University, Taoyuan City, Taiwan

ARTICLE INFO

Keywords:
Electrospinning
Polypeptides
$Ti_3C_2T_x$ MXene
Interfacial polarity
Mechanical reinforcement
Nanocomposites

ABSTRACT

Developing predictive design principles for $Ti_3C_2T_x$ MXene–polymer composites requires a fundamental understanding of how interfacial polarity governs mechanical response. Here, we systematically interrogate this relationship using a homologous series of electrospun polypeptide fibers with tunable polarity: hydrophobic poly(γ-benzyl-L-glutamate) (PBG), intermediate-polarity PBGA15 (30% hydrolyzed PBG), and highly hydrophilic poly(γ-(4-carbobenzoxy-L-lysine)-*co*-γ-benzyl-L-glutamate (7CBZL3BG, 70%CBZL and 30%BG). Across this polarity gradient, we identify three distinct mechanical regimes controlled by matrix-filler interactions. Specifically, the hydrophobic PBG system suffers from aggregation-driven degradation caused by severe polarity mismatch. In contrast, the intermediate PBGA15 achieves strength-dominated reinforcement via efficient interfacial load transfer, while the hydrophilic 7CBZL3BG exhibits ductile toughening mediated by dynamic, reversible interfacial sliding. The universality of this polarity-governed framework is confirmed through external validation with commercial polycaprolactone (PCL) and poly(vinyl alcohol) (PVA). Furthermore, biological assays with PC-12 cells demonstrate excellent cytocompatibility, with fiber alignment offering effective contact guidance for cellular orientation. These findings establish interfacial polarity matching as a key design parameter for tailoring the mechanical and biological functions of structural nanocomposites.

1. Introduction

Polypeptide-based synthetic polymers have garnered significant attention as functional platforms for tissue engineering and structural composites, owing to their programmable molecular architecture, tunable side-chain chemistry, and intrinsic biocompatibility [1–3]. Among these, poly(γ-benzyl-L-glutamate) (PBG) and its deprotected derivatives offer a versatile library for constructing electrospun fibers with controllable secondary structures [4,5]. The inherent α-helical backbone of these polypeptides imparts exceptional stiffness and molecular ordering; however, this rigidity often compromises extensibility, leading to brittle fracture under tensile load [6–9]. Consequently, enhancing the mechanical robustness of polypeptide fibers without sacrificing their molecular precision remains a central challenge in expanding their utility for advanced functional applications.

Electrospinning provides a robust pathway to fabricate micro- to nanoscale fibers with tunable alignment and porosity [10,11]. While aligned fibrous mats can exhibit anisotropic stiffness due to molecular orientation [12–14], their macroscopic performance is critically governed by the interfacial interactions between the polymer matrix and incorporated nanofillers [15,16]. Even subtle variations in matrix polarity, hydrogen-bonding capability, or surface chemistry can drastically alter jet stability and stress-transfer mechanisms. Therefore, rational engineering of the polymer-filler interface is essential to achieve predictable and application-relevant mechanical behaviors in composite systems.

☆ This article is part of a Special issue entitled: 'TACT2025' published in Surface & Coatings Technology.

* Correspondence to: P.-C. Chen, Institute of Materials Science and Engineering, National Taipei University of Technology, Taipei City, Taiwan.
** Correspondence to: Y-C. Huang, Department of Materials Engineering and Biochemical Technology R&D Center, Ming Chi University of Technology, New Taipei City, Taiwan.
E-mail addresses: cpc@ntut.edu.tw (P.-C. Chen), huangyc@mail.mcut.edu.tw (Y.-C. Huang).

https://doi.org/10.1016/j.surfcoat.2026.133622
Received 3 January 2026; Received in revised form 3 April 2026; Accepted 23 May 2026
Available online 28 May 2026

In this context, two-dimensional transition metal carbides (MXenes), particularly $Ti_3C_2T_x$, have emerged as highly promising nanofillers. Their high aspect ratio, metallic conductivity, and abundant surface terminations (-OH, —O, —F) make them ideal candidates for interfacial engineering [17–20]. Previous studies have reported MXene-induced enhancements in conductivity [21–23], thermal stability [24,25], and mechanical reinforcement [26–29] in various polymer matrices such as poly(vinyl alcohol) (PVA), polycaprolactone (PCL), and polyacrylonitrile (PAN). However, current understanding is largely derived from isolated studies focusing on specific and high-polarity polymers. Relying on such trial-and-error additive approaches is fundamentally insufficient, as it fails to capture the underlying interfacial dynamics when matrix chemistry changes. Without a unified predictive framework, the design of MXene composites carries significant scientific and industrial risks, such as unpredictable macroscopic failures in load-bearing tissue scaffolds [23] or premature interfacial delamination in neuro-prosthetic devices [30]. A systematic investigation into how polarity matching across a continuous chemical spectrum governs nanosheet dispersion and the resulting reinforcement mechanism remains notably absent. Furthermore, while low filler loadings typically improve performance, aggregation at higher loadings or interfacial saturation often leads to premature failure [31–33], highlighting the need for a unified mechanistic framework.

To address this gap, this study utilizes a homologous series of polypeptides to systematically interrogate the role of interfacial polarity. We employ hydrophobic PBG, intermediate-polarity PBGA15 (partially deprotected), and highly hydrophilic 7CBZL3BG (fully deprotected) as a model system. This platform allows for the precise modulation of interfacial interactions with fluoride-free $Ti_3C_2T_x$ MXene while maintaining a consistent backbone architecture. We hypothesize that interfacial polarity does not merely influence dispersion quality but plays a dominant role in governing the transition between three distinct mechanical regimes: (1) aggregation-driven degradation in hydrophobic matrices; (2) strength-based reinforcement via effective load transfer; and (3) ductile toughening mediated by reversible interfacial sliding. Herein, we report a comprehensive evaluation of MXene-reinforced electrospun fibers across this polarity gradient. By correlating dispersion states, crystallographic evolution, and wetting behaviors with tensile properties, we validate the polarity-governed mechanisms. These findings are further corroborated using commercial reference polymers, PCL and PVA, to demonstrate the universality of the proposed design principles. Finally, given the potential of these materials as functional scaffolds, the biological implications of polarity-driven interfaces are assessed via cytocompatibility assays. This work establishes a predictive guideline for tailoring the mechanical and biological functions of MXene-polymer composites through precise interfacial engineering.

2. Experimental section

2.1. Materials

The MAX phase precursor, Ti_3AlC_2 powder (purity ≥98%, CAS No. 159606–79-0), and sodium hydroxide (NaOH, ≥ 97%) were purchased from Sigma-Aldrich (USA). Tetrahydrofuran (THF, reagent grade, ≥ 99.8%) was supplied by J.T. Baker (USA), and *N*,*N*-dimethylacetamide (DMAc, ≥ 99.5%) was obtained from ACROS Organics (Belgium). Three polypeptide-based polymers were synthesized in-house: (1) PBG (poly(γ-benzyl-L-glutamate)), a moderately hydrophobic polypeptide; (2) PBGA15, a partially deprotected copolypeptide with intermediate hydrophilicity; and (3) 7CBZL3BG (poly(70% γ-(4-carbobenzoxy-L-lysine)-co-30% γ-benzyl-L-glutamate)), a hydrophilic copolypeptide. All commercial reagents were used as received without further purification.

2.2. Fluorine-free hydrothermal synthesis of MXene

$Ti_3C_2T_x$ MXene was synthesized via a fluoride-free, alkali-assisted hydrothermal etching route [17]. In a typical procedure, 500 mg of Ti_3AlC_x powder was dispersed in 70 mL of 27.5 M NaOH solution and transferred to a 100 mL Teflon-lined stainless-steel autoclave. The reaction was maintained at 270 °C for 72 h. After cooling to room temperature, the suspension was washed repeatedly with deionized water via centrifugation (4000 rpm, 10 min, 5 cycles) until the supernatant pH reached ≈ 7. The resulting sediment was redispersed in water and ultrasonicated for 30 min to promote nanosheet delamination. Based on the morphological characterizations reported for this specific alkali-treatment protocol [17], the delaminated MXene typically exists as few-layer stacks with an average lateral size of 80–200 nm and a thickness of 8–25 nm. This sub-micron, high-aspect-ratio geometry provides the essential structural prerequisite for efficient interfacial stress transfer within the electrospun fibers. The final $Ti_3C_2T_x$ product was collected and vacuum-dried. This fluoride-free protocol yields MXene enriched with oxygen-containing surface terminations (-O/-OH), enhancing its aqueous dispersibility and compatibility with polar polymer matrices. Crucially, compared to traditional HF-etched MXenes, the elimination of hydrogen-bond-inactive fluorine (—F) terminations maximizes the intrinsic polarity of the nanosheets. This exceptionally high density of -OH and —O groups provides a concentrated platform for dynamic hydrogen bonding, making the matrix–filler interfacial interactions exquisitely sensitive to the systematic polarity gradient of the polypeptide series investigated in this study.

2.3. Synthesis of polypeptides

PBG, partially deprotected PBGA15, and the copolypeptide 7CBZL3BG were synthesized following our previously reported N-carboxyanhydride (NCA) ring-opening polymerization procedures [20]. While the general synthetic routes and purification steps were identical to those described in our earlier publications, specific reaction parameters were controlled to target distinct polarities. Briefly, PBG and 7CBZL3BG (7:3 M ratio) were polymerized in benzene at 25 °C. To obtain the intermediate-polarity PBGA15, PBG was treated with HBr/acetic acid in 1,2-dichloroethane (DCA) at 31 °C for exactly 45 min. To ensure molecular consistency and reproducibility, the synthesized polymers were characterized by GPC and ^{1}H NMR (see Fig. S1 and Fig. S2 in Supporting Information). The GPC results show that the PBG matrix has an Mn of 445.0 kDa and an Mw of 590.5 kDa (PDI = 1.33), while the 7CBZL3BG has an Mn of 727.7 kDa and an Mw of 1084.4 kDa (PDI = 1.49). Furthermore, based on 1H NMR analysis, the actual degree of hydrolysis for the partially deprotected matrix was determined to be 13.8–15.5%. Therefore, to accurately reflect its chemical composition, this intermediate-polarity variant is designated as PBGA15 in the subsequent sections of this study. For clarity, this study utilizes PBG as the hydrophobic baseline, PBGA15 as the intermediate-polarity variant, and 7CBZL3BG as the hydrophilic copolypeptide, enabling controlled polarity modulation across a consistent backbone.

2.4. Electrospinning of polypeptide/MXene composite fibers

Electrospinning solutions were prepared based on the solubility and polarity of the respective matrices. PBG and PBGA15 were dissolved in a THF/DMAc mixture (7:3 *v*/v) at a concentration of 15 wt%. The hydrophilic 7CBZL3BG was dissolved in acetone/DMAc (2:1 v/v) at 30 wt %. For composite fibers, $Ti_3C_2T_x$ MXene was first dispersed in the solvent system via ultrasonication, then blended with the polymer solutions to achieve loadings of 0.5, 1.0, and 1.5 wt% (relative to polymer weight). It should be noted that the MXene loading was intentionally kept at ≤1.5 wt%. This range was selected to capture the optimal mechanical reinforcement window while avoiding the processing limitations and severe aggregation onset that typically occur at higher MXene concentrations in electrospinning. Achieving electrical percolation was not the primary objective of this structural and biological optimization. All solutions were magnetically stirred for 15 h and degassed prior to

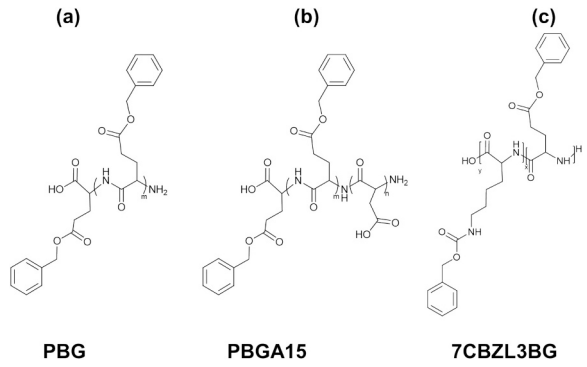

Fig. 1. Schematic illustration of the polypeptide structures: (a) PBG, (b) PBGA15, and (c) 7CBZL3BG.

spinning. Electrospinning was performed using a metallic needle tip at an applied voltage of 20 kV and a tip-to-collector distance of 10 cm. The solution flow rate was controlled at 5.0 mL/h for PBG and PBGA15, and 6.0 mL/h for 7CBZL3BG. Aligned nanofibers were collected on a rotating drum (1800 rpm). Environmental conditions were maintained at 25 °C and 40–45% relative humidity. To simplify comparison across different compositions, composite samples are designated as "Polymer-X", where X denotes the MXene loading (wt%) relative to the polymer mass.

2.5. Characterization

The morphology and structural features of MXene and MXene-polypeptide composite fibers were characterized using multiple analytical techniques. Scanning electron microscopy (SEM, Hitachi S-3400 N, Japan) was used to examine the fiber surface morphology and alignment, with the instrument operating at an accelerating voltage of 5–10 kV. Prior to imaging, MXene samples were sputter-coated with Au (approximately 5 nm in thickness) to enhance surface conductivity. X-ray diffraction (XRD, Rigaku MiniFlex, Japan) was used to confirm the layered structure of $Ti_3C_2T_x$ MXene and to evaluate crystalline features within the composite fibers. Cu Kα radiation ($\lambda = 1.5406$ Å) was used as the X-ray source, operated at 40 kV and 30 mA. Data were collected over a 2θ range of 3–70° with a scanning rate of 2°/min. The hydrophilicity of the fiber mats was assessed via static water contact angle measurements (Pentad Scientific Corporation, Taiwan). A 5 μL droplet of deionized water was dispensed onto three independent locations on each sample, and the average value was reported to represent surface wettability. Mechanical properties were evaluated using a texture analyser (TA. XTplusC, Stable Micro Systems, UK). Fiber mats were cut into rectangular strips (10 mm × 50 mm × thickness = 50 μm), and tensile tests were conducted at a crosshead speed of 5 mm/min at room temperature. Each measurement was repeated at least three times to ensure statistical reliability. Young's modulus, tensile strength, and elongation at break were determined from the corresponding stress-strain curves.

3. Results and discussion

Fig. 1 illustrated the chemical structures of the polypeptide matrices used in this study, highlighting a controlled variation in side-chain chemistry that gives rise to distinct polarity levels. Poly(γ-benzyl-L-glutamate) (PBG) lies at the low-polarity end of the series, as its side chains are predominantly composed of benzyl-protected groups. In PBGA15, partial modification of the side chains introduces additional polar functionalities while a considerable fraction of hydrophobic moieties is retained, leading to an intermediate-polarity matrix. By contrast, 7CBZL3BG contains a much higher proportion of polar functional groups along the side chains, and therefore exhibits the highest overall polarity among the three polymers. Notably, the polypeptide backbone remains identical across all systems, ensuring that the differences observed in subsequent analyses can be primarily attributed to side-chain polarity rather than changes in backbone architecture.

Fig. 2a presents the SEM microstructure, revealing a distinct stacked, sheet-like architecture. The visible delamination between layers suggests the effective extraction of Al from the MAX phase precursor, resulting in a loosened lamellar structure characteristic of alkali-etched MXenes [7]. Complementing this morphological assessment, the EDS spectrum (Fig. 2b) confirms the compositional purity of the nanosheets. The profile is dominated by Ti, C, and O signals, whereas the Al peak is negligible, indicating near-complete etching. The detection of a minor Na signal is attributed to the intercalation of sodium ions between the layers during the hydrothermal process, which has been reported to facilitate interlayer expansion in alkali-treated MXenes [17]. The XRD patterns in Fig. 2c further confirm this structural transformation. A significant shift of the (002) reflection was observed, moving from $2\theta \approx 9.2°$ in pristine Tix_3AlC_2 to $\approx 7.2°$ in the treated sample. According to Bragg's law, this shift corresponds to an increase in d-spacing from ~9.6 Å to ~12.3 Å, validating the successful opening of the gallery space by -OH/-O functional groups and intercalated cations. Furthermore, the diminished intensity of the non-basal (104) and (105) peaks provides evidence of a transition toward a turbostratic stacking order, confirming the conversion into high-quality $Ti_3C_2T_x$ sheets ready for composite fabrication [21].

Fig. 3 illustrates the surface morphology of electrospun polypeptide fibers incorporating varying MXene loadings. Across all three polymer matrices, continuous and bead-free fibrous architectures were successfully obtained, confirming stable processing conditions. Although the average fiber diameters remained within the 0.78–1.18 μm range, distinct polarity-dependent variations in uniformity and surface texture were observed. These differences reflect the competitive interplay between solution conductivity, interfacial compatibility, and jet stability during the electrospinning process. In the hydrophobic PBG matrix, a

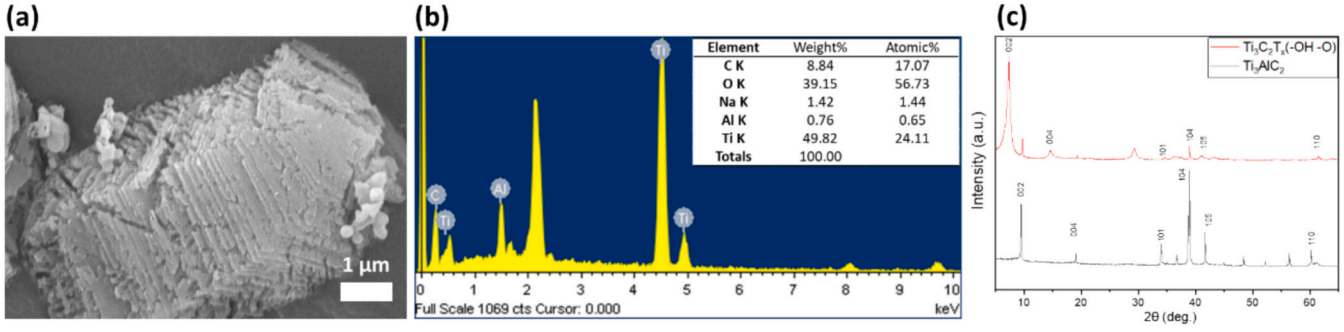

Fig. 2. Morphological and structural characterization of the fluoride-free $Ti_3C_2T_x$ MXene. (a) SEM micrograph revealing the characteristic stacked, sheet-like morphology after NaOH-assisted hydrothermal treatment. (b) EDS elemental analysis confirming the effective removal of Al and the predominance of Ti, C, and O elements. (c) XRD patterns illustrating the crystallographic shift of the (002) plane and the phase transformation from the Ti_3AlC_2 precursor to $Ti_3C_2T_x$.

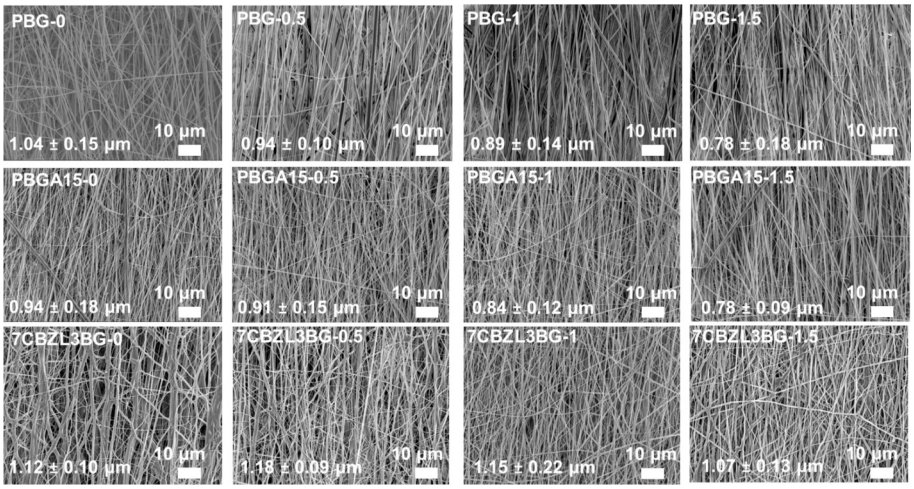

Fig. 3. SEM images of electrospun fibers with varying MXene.

monotonic reduction in fiber diameter was noted with increasing MXene content. This thinning effect is largely attributed to by the enhanced solution conductivity imparted by the conductive nanosheets, which intensifies the extensional forces on the jet. However, at higher loadings (1.5 wt%), the polarity mismatch between the non-polar PBG backbone and the hydrophilic -OH/-O-terminated MXene promotes nanosheet aggregation. This phase separation induces localized jet instabilities and incomplete solvent evaporation, resulting in partial fiber fusion and surface wrinkling rather than classical bead formation.

In contrast, the PBGA15 matrix exhibits superior morphological uniformity and the narrowest diameter distribution. The partial deprotection of PBGA introduces specific -COOH and -NH_2 moieties along the backbone, facilitating favorable hydrogen bonding and electrostatic interactions with the MXene surface. These interfacial forces effectively anchor the nanosheets, preventing aggregation and stabilizing the jet. Consequently, jet elongation proceeds homogeneously, yielding smooth, defect-free fibers. The absence of fusion or surface irregularities suggests that PBGA15 achieves an optimal balance between electrical stretching forces and interfacial cohesion. For the highly hydrophilic 7CBZL3BG system, the abundance of ionizable side chains fosters a robust hydrogen-bonded network between the polymer chains and MXene sheets. This molecular-level interaction not only suppresses aggregation but also homogenizes local viscosity and charge distribution, maintaining jet integrity even at high filler loadings. While the overall morphology remains highly stable, a slight increase in diameter variability suggests a transition into a regime dominated by strong intermolecular associations. Among these systems, PBGA15 represents a mechanically favorable regime in which interfacial interactions and nanosheet dispersion are synchronized. Before discussing the macroscopic mechanical properties, it is crucial to establish the physical bridge between matrix polarity and filler dispersion quality. The surface morphological features in Fig. 3 serve as reliable macroscopic indicators of the underlying dispersion states. In the hydrophobic PBG matrix, the observed surface wrinkling and partial fiber fusion at higher loadings are direct manifestations of severe internal MXene agglomeration caused by polarity mismatch. In contrast, the smooth, uniform architectures of the PBGA15 and 7CBZL3BG fibers suggest favorable dispersion. To directly confirm this, EDS elemental mapping was conducted (Fig. S1, Supporting Information). As a baseline control, the pure 7CBZL3BG fibers exhibited no detectable Titanium (Ti) signal. Upon the addition of 0.5 wt% MXene, a highly uniform distribution of the Ti signal emerged across the fibrous network. This visually confirms the homogeneous dispersion of MXene nanosheets facilitated by interfacial polarity matching. This polarity-driven uniform dispersion prevents the formation of structural defect centers and provides an optimized, continuous network for effective interfacial load transfer. Consequently, these distinct internal dispersion states directly dictate the divergent mechanical reinforcement pathways observed in the subsequent tensile evaluations.

To quantify these structure-property relationships, tensile stress-strain curves of the composite fibers were evaluated, as shown in Fig. 4. Despite the identical intrinsic rigidity of the MXene filler, the three polymer matrices exhibit fundamentally divergent mechanical responses. This observation suggests that the reinforcement mechanism is complex and primarily governed by the matrix-filler interplay, rather than filler content alone. In the hydrophobic PBG system (Fig. 4a), a monotonic decline in Young's modulus, tensile strength, and elongation at break was observed with increasing MXene content. This trend

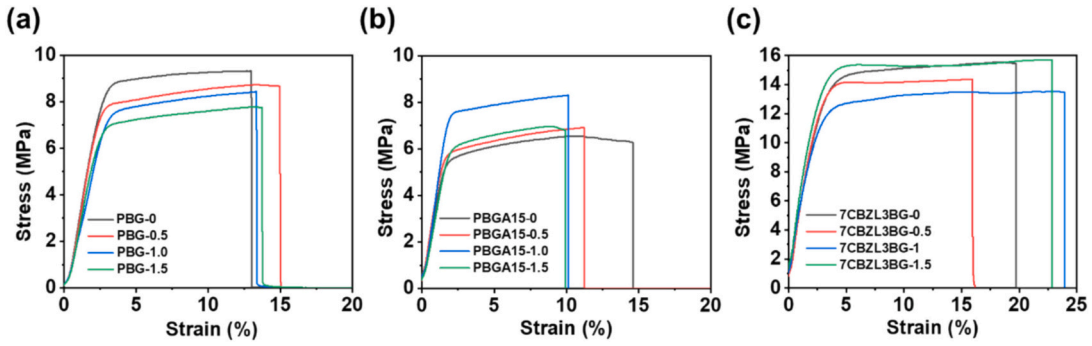

Fig. 4. Tensile stress-strain curves of electrospun composite scaffolds based on (a) PBG, (b) PBGA15, and (c) 7CBZL3BG matrices reinforced with varying MXene loadings (0, 0.5, 1.0, and 1.5 wt%).

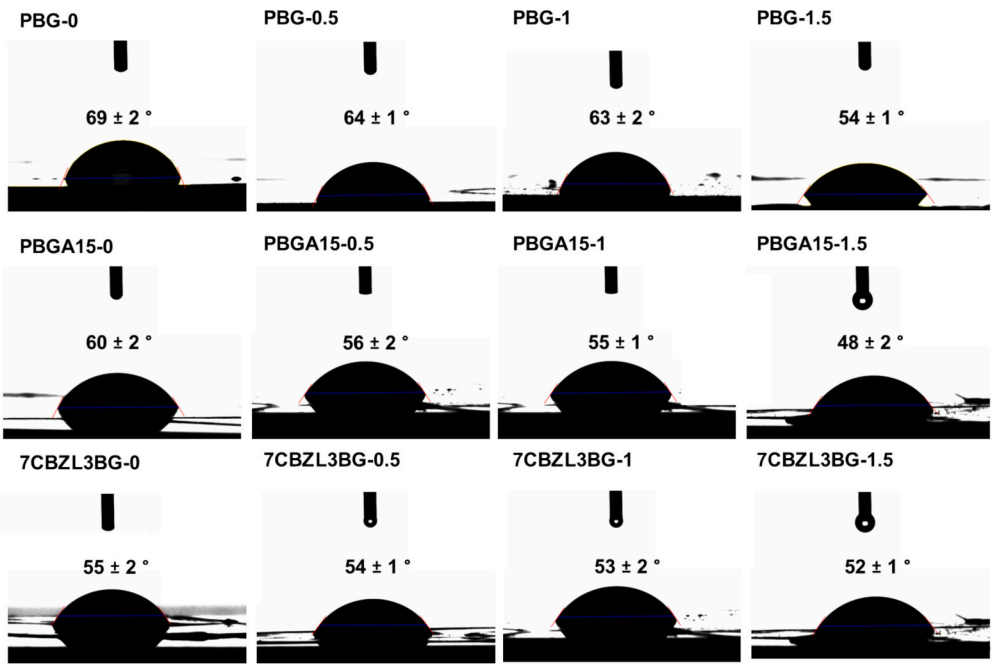

Fig. 5. Variation of static water contact angles for PBG, PBGA15, and 7CBZL3BG composite films as a function of $Ti_3C_2T_x$ MXene loading (0–1.5 wt%).

typifies an aggregation-dominated degradation mechanism. Due to the severe polarity mismatch between the PBG backbone and the hydrophilic MXene, interfacial adhesion is inherently weak. As loading increases, rigid filler clusters form, acting as stress concentrators rather than load-bearing elements. Consequently, stress accumulation at matrix-filler debonding sites is expected to promote premature crack initiation and propagation. This progressive failure mechanism explains the simultaneous deterioration of stiffness and ductility. In contrast, the PBGA15 system, as shown in Fig. 4b, demonstrates a classical reinforcement profile dominated by effective load transfer. At low loadings (0.5 wt%), significant enhancements in both modulus and strength are achieved while maintaining ductility. Here, the -COOH and -NH_2 groups on the PBGA15 backbone establish strong hydrogen bonding and electrostatic anchors with the MXene surface. These interactions minimize interfacial slippage, allowing efficient stress transmission to the rigid nanosheets. However, at higher loadings (1.0 to 1.5 wt%), the mechanical response deteriorates due to interfacial saturation and nanosheet overlap. This non-monotonic behavior reflects a trade-off between interfacial reinforcement and the disruption of polymer chain continuity by excessive filler. Conversely, the highly polar 7CBZL3BG system (Fig. 4c) exhibits a toughness-dominated response. While the modulus remains nearly invariant, the elongation at break increases markedly with MXene content. The high density of functional side chains facilitates a dynamic, reversible hydrogen-bonding network with the nanosheets. Under tension, mechanisms such as interfacial sliding, nanosheet rotation, and partial pull-out are activated, effectively dissipating mechanical energy and delaying catastrophic failure. This suggests a regime governed by interfacial rearrangement and energy dissipation rather than rigid-filler percolation. Although direct visual confirmation of these nanoscale events (e.g., nanosheet pull-out) at the fracture surface is hindered by the extensive plastic deformation and macroscopic necking of the highly ductile matrix (as shown in the representative post-fracture morphology, Fig. S4, Supporting Information), this interfacial sliding mechanism is robustly substantiated. It is primarily deduced from the distinct macroscopic mechanical fingerprint—specifically, the massive increase in elongation and toughness—and is structurally supported by the uniform MXene dispersion confirmed via EDS mapping (Fig. S3). Ultimately, these results delineate three distinct mechanical regimes driven by matrix polarity, ranging from aggregation-induced failure in hydrophobic PBG to strength-based reinforcement in PBGA15, and finally, ductile toughening in the polar 7CBZL3BG system. This confirms that matching interfacial polarity is the decisive parameter for tailoring the mechanical functions of electrospun MXene–polypeptide composites.

The impact of MXene incorporation on surface wettability was evaluated via static water contact angle measurements, as presented in Fig. 5. Across all three systems, a monotonic increase in hydrophilicity was observed with increasing filler content, which can be attributed to a trend driven by the surface exposure of the $Ti_3C_2T_x$ nanosheets. The abundant polar -OH and —O terminations on the MXene surface effectively increase the surface free energy, thereby promoting water spreading. This behavior is consistent with previous reports on MXene-termination-governed wetting, such as the progressive contact angle reduction observed in cellulose acetate/MXene composites (e.g., decreasing from ~71° to ~48°) [29]. Notably, the hydrophobic PBG system undergoes the most drastic surface energy modification, with the contact angle dropping significantly from 69 ± 2° to 54 ± 1°. Although intrinsic PBG is hydrophobic, the introduction of MXene creates localized hydrophilic domains at or near the fiber surface that can disrupt the water-solid interface, leading to a substantial enhancement in wettability. Similarly, the PBGA15 system exhibits a marked increase in hydrophilicity, reaching the lowest absolute contact angle value among all groups (48 ± 2°). The partially deprotected PBGA15 backbone, rich in -COOH and -NH_2 groups, is expected to facilitate the uniform dispersion of MXene through hydrogen bonding. This synergistic interaction ensures that the hydrophilic filler is effectively presented at the material surface, maximizing the wettability modulation. In contrast, the 7CBZL3BG system displays a distinct “saturation” behavior, showing only a marginal decline in contact angle from 55 ± 2° to 52 ± 1°. Since the pristine polymer surface is already highly polar due to the high density of ionizable side chains, the addition of MXene primarily modifies the internal bulk structure rather than significantly altering the already hydrophilic surface chemistry. This observation aligns with studies on other inherently hydrophilic matrices, where the initial static contact angle remains less sensitive to MXene content, even though dynamic wetting behavior may still be affected [25,26]. These distinct wetting profiles reflect the intrinsic matrix polarity and the degree of surface-accessible MXene, correlating well with the mechanical regimes

Table 1
Physical, mechanical, and surface properties of peptide/MXene composite fibers.

Sample	Fiber diameter (μm)	Young's modulus (MPa)	Elongation (%)	Thickness (μm)	Contact angle (°)
PBG-0	1.04 ± 0.15	152 ± 32	12 ± 2	50	69 ± 2
PBG-0.5	0.94 ± 0.10	143 ± 17	13 ± 1	50	64 ± 1
PBG-1.0	0.89 ± 0.14	132 ± 24	14 ± 1	55	63 ± 2
PBG-1.5	0.78 ± 0.18	124 ± 18	13 ± 2	52	54 ± 1
PBGA15–0	0.94 ± 0.18	275 ± 27	14 ± 1	54	60 ± 2
PBGA15–0.5	0.91 ± 0.15	324 ± 42	15 ± 1	50	56 ± 2
PBGA15–1.0	0.84 ± 0.12	285 ± 22	11 ± 1	52	55 ± 1
PBGA15–1.5	0.78 ± 0.09	233 ± 15	10 ± 1	53	48 ± 2
7CBZL3BG-0	1.12 ± 0.10	424 ± 40	19 ± 2	52	55 ± 2
7CBZL3BG-0.5	1.18 ± 0.09	453 ± 19	15 ± 2	55	54 ± 1
7CBZL3BG-1.0	1.15 ± 0.22	485 ± 48	23 ± 1	54	53 ± 2
7CBZL3BG-1.5	1.07 ± 0.13	429 ± 45	22 ± 1	53	52 ± 1

discussed earlier. To provide a comprehensive overview of the structure–property relationships, the key physical parameters of all composite systems are summarized in Table 1.

To further validate the hypothesis that matrix polarity dictates the MXene reinforcement mechanism, commercial hydrophobic polycaprolactone (PCL) and hydrophilic poly(vinyl alcohol) (PVA) were examined as external reference systems, and the results are shown in Fig. 6. For each polymer, pristine PCL and PVA (0 wt%) and composite films (1 wt% $Ti_3C_2T_x$, named as PCL-1.0 and PVA-1.0) were prepared, with thickness carefully controlled within 50–56 μm to minimize measurement artifacts. Consistent with the wetting behavior observed in the polypeptide systems, the water contact angle (Fig. 6a) of hydrophobic PCL decreased notably from 72 ± 1° to 68 ± 2° upon MXene incorporation. This result confirms that even minor exposure of polar -OH/ —O terminations is sufficient to modify the surface energy of intrinsically hydrophobic matrices. In contrast, the hydrophilic PVA showed a muted response, with the contact angle decreasing only slightly from 26 ± 2° to 23 ± 1°, mirroring the saturation effect observed in the 7CBZL3BG system due to its pre-existing surface polarity [14]. From a mechanical perspective, the stress-strain behaviors (Fig. 6b) of these control systems further corroborate the polarity-driven regimes, as listed in Table 2. In the hydrophobic PCL matrix, the incorporation of 1 wt% $Ti_3C_2T_x$ induced a brittle failure mode, with Young's modulus dropping from 82 ± 5 MPa to 24 ± 4 MPa and elongation at break reducing from 38 ± 2% to 21 ± 2%. This degradation parallels the PBG system and is consistent with poor interfacial compatibility and stress concentration induced by aggregation. Conversely, the hydrophilic PVA matrix exhibited a toughening response similar to that of 7CBZL3BG. While the modulus decreased moderately (from 152 ± 9 MPa to 114 ± 8 MPa), the elongation at break increased from 60 ± 8% to 72 ± 5%. The extended post-

Table 2
Physical, mechanical, and surface properties of polymer fibers with and without MXene incorporation.

Sample	Young's modulus (MPa)	Elongation (%)	Thickness (μm)	Contact angle (°)
PCL-0	82 ± 5	38 ± 2	56	72 ± 1
PCL-1.0	24 ± 4	21 ± 2	52	68 ± 2
PVA-0	152 ± 9	60 ± 8	50	26 ± 2
PVA-1.0	114 ± 8	72 ± 5	54	23 ± 1

necking deformation indicates enhanced energy dissipation, which is attributed to reversible hydrogen bonding and electrostatic interactions between the PVA side groups and MXene terminations. These interactions facilitate interfacial sliding or partial nanosheet pull-out under tension, thereby increasing ductility without catastrophic strength loss [31]. Regarding the observed reduction in Young's modulus, this deviation from conventional rigid reinforcement can be attributed to the interference with the intrinsic semi-crystallinity of the PVA matrix. Pristine PVA possesses a high modulus driven by a highly ordered crystalline network formed through strong intermolecular hydrogen bonding. Upon the introduction of MXene, its abundant surface terminations (-OH, —O, and —F) engage in competitive interfacial hydrogen bonding with the PVA chains. As established in a previous study [34], these competitive interactions disrupt the native PVA-PVA hydrogen bonds, hindering the tight packing of the polymer chains and effectively reducing the overall crystallinity of the matrix. Consequently, this structural "plasticization" effect leads to the macroscopic decrease in the elastic modulus, even as the dynamic MXene-PVA interactions concurrently enhance ductility. Ultimately, these findings confirm that the matrix-filler polarity match is a universal governing factor, uniformly distinguishing aggregation-prone degradation in hydrophobic matrices from interfacial toughening in hydrophilic systems. It is important to note that while the concept of interfacial polarity matching is a general design rule, the specific realization of the ductile toughening regime relies heavily on the capacity for dynamic interfacial interactions. Therefore, this framework is primarily applicable to polar or hydrogen-bond-capable matrices. For entirely nonpolar polymer systems lacking functional interaction sites, the severe polarity mismatch with MXene would default to the aggregation-driven degradation regime, necessitating the use of interfacial compatibilizers to bridge the polarity gap.

Following the structural and mechanical analyses, the potential of these scaffolds for cell-material interaction assessments relevant to tissue engineering applications was examined via in vitro cell culture. The viability and morphology of PC-12 cells were monitored after 3 and 7 days (Fig. 7). At day 3, all composite scaffolds displayed predominant green fluorescence with negligible red signals, confirming high initial cytocompatibility across all substrates. The relatively sparse cell distribution at this early stage indicates that the cells were in the initial phase of attachment and acclimation, a behavior commonly observed during

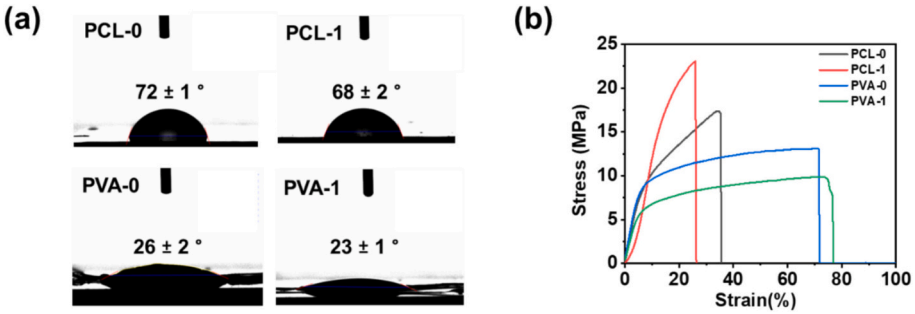

Fig. 6. Wettability and mechanical behavior of PCL and PVA matrices with and without MXene incorporation. (a) Water contact angle images of pristine (0 wt%) and 1 wt% MXene-loaded samples. (b) Tensile stress–strain curves of PCL and PVA matrices at 0 and 1 wt% MXene.

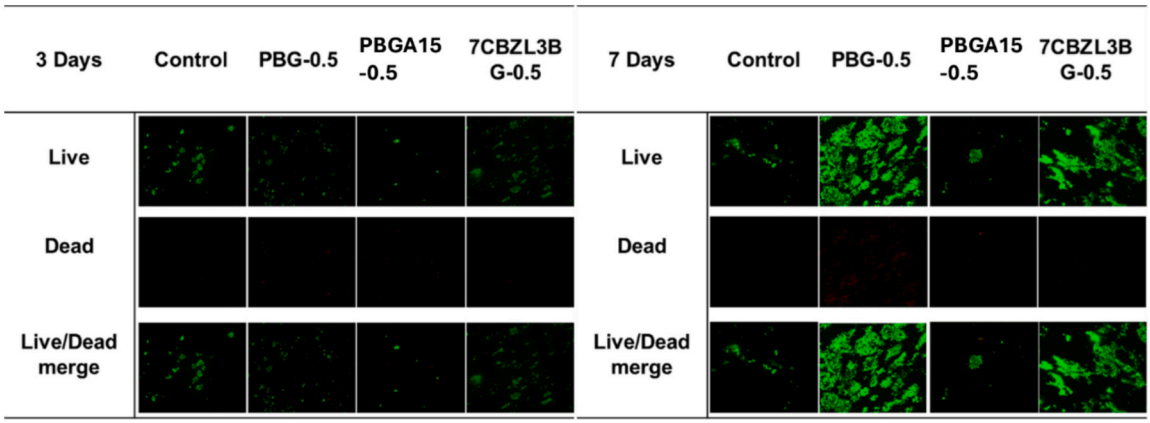

Fig. 7. Fluorescence images of PC-12 cells on different polypeptide/MXene scaffolds at day 3 and day 7. Green: live cells; Red: dead cells; and Merge.

early culture on fibrous substrates. By day 7, however, proliferation behaviors diverged significantly based on matrix chemistry. The control, PBG, and 7CBZL3BG systems (loaded with 0.5 wt% MXene) supported robust cell growth, characterized by increased cell density and distinct cellular alignment along the fiber axis. This alignment confirms that the fibrous architecture effectively provides contact guidance cues to direct neurite extension. Conversely, the PBGA15-based fibers exhibited noticeably lower cell colonization. This suppression is structurally attributed to the 13.8–15.5% degree of hydrolysis in the PBGA15 matrix, which generates abundant deprotected carboxylic acid (-COOH) groups. Because cell membranes are inherently negatively charged [35], these -COOH groups impart a strong negative surface potential to the fibers, driving significant electrostatic repulsion. Synergizing with the localized acidity created by proton donation, this repulsion alters the conformation of adsorbed cell-adhesive proteins (e.g., fibronectin), thereby hindering initial cell attachment and stable focal adhesion formation. Importantly, the persistent absence of red fluorescence across all samples confirms that the reduced cell coverage originates from unfavorable interfacial adhesion characteristics rather than cytotoxicity. This phenomenon highlights a critical trade-off in composite scaffold design: optimal mechanical reinforcement and biological performance are not necessarily aligned. While the intermediate polarity of PBGA15 provides ideal interfacial load transfer for maximizing tensile strength, its acidic surface hinders optimal cellular attachment. For future biomedical applications requiring both high structural integrity and superior cytocompatibility, this trade-off could be reconciled through targeted surface modifications of the PBGA15/MXene scaffolds. Strategies such as post-spinning functionalization with cell-adhesive peptides or controlled adsorption of extracellular matrix proteins could effectively mask the acidic residues and promote cell focal adhesion without compromising the bulk mechanical advantages provided by the matrix-filler interface.

4. Conclusion

This study establishes a unified interfacial framework describing how matrix polarity governs the mechanical, structural, and biological responses of MXene-polymer composite fibers. By utilizing a homologous series of polypeptides with progressively increasing polarity, we demonstrate that fluoride-free $Ti_3C_2T_x$ MXene induces three distinct reinforcement regimes: aggregation-driven mechanical deterioration in hydrophobic matrices, efficient load transfer and strength enhancement in moderately polar systems, and ductile toughening enabled by reversible interfacial interactions in highly hydrophilic matrices. These polarity-dependent behaviors correlate with nanosheet dispersion quality, wetting characteristics, and surface-exposed functional groups, and are further validated using commercial PCL and PVA as external references. Importantly, all MXene–polypeptide composites exhibit high cytocompatibility, with aligned fibers promoting contact-guided cellular orientation. Collectively, these results highlight interfacial polarity as a decisive and generalizable parameter for engineering MXene-based fibrous composites, offering a predictive guideline for optimizing their mechanical integrity and biological performance in structural and tissue engineering applications.

CRediT authorship contribution statement

Yu-Yuan Ku: Writing – original draft, Visualization, Validation, Methodology, Investigation, Formal analysis. **Meng-Fang Lin:** Supervision, Resources, Funding acquisition. **Tsui-Yun Chung:** Investigation, Formal analysis, Data curation. **Yu-Ting Lin:** Investigation, Data curation. **Wen-Han Tsao:** Investigation, Data curation. **Jun Ohta:** Conceptualization. **Wei-Fang Su:** Writing – review & editing, Supervision. **Po-Chun Chen:** Writing – review & editing, Supervision, Project administration, Funding acquisition, Conceptualization. **Yu-Ching Huang:** Writing – review & editing, Supervision, Project administration, Funding acquisition, Conceptualization.

Declaration of competing interest

The authors declare the following financial interests/personal relationships which may be considered as potential competing interests: Po-Chun Chen reports financial support was provided by National Science and Technology Council, Taiwan. If there are other authors, they declare that they have no known competing financial interests or personal relationships that could have appeared to influence the work reported in this paper.

Acknowledgments

This research was supported in full by the National Science and Technology Council of Taiwan (Grant numbers: NSTC 114-2221-E-131-012-MY3, 114-2221-E-131-038, 113-2221-E-027-012-MY3, 112-2628-E-131-001-MY4).

Appendix A. Supplementary data

Supplementary data to this article can be found online at https://doi.org/10.1016/j.surfcoat.2026.133622.

Data availability

Data will be made available on request.

References

[1] N. Qiang, W. Lin, X. Zhou, Z. Liu, M. Lu, S. Qiu, S. Tang, J. Zhu, Gels 7 (2021) 196.
[2] Z. Geng, T. Laakko, A. Hokkanen, C. Södergård, I. Maasilta, P. Mohammadi, Commun. Mater. 5 (2024) 152.
[3] X. Wang, M. Mondal, P.E. Jankoski, L.K. Kemp, T.D. Clemons, V. Rangachari, S. E. Morgan, ACS Appl. Polym. Mater. 7 (2025) 3739.
[4] M. Naguib, M. Kurtoglu, V. Presser, J. Lu, J. Niu, M. Heon, L. Hultman, Y. Gogotsi, M.W. Barsoum, Adv. Mater. 23 (2011) 4248.
[5] A. Lipatov, H. Lu, M. Alhabeb, B. Anasori, A. Gruverman, Y. Gogotsi, A. Sinitskii, Sci. Adv. 4 (2018) eaat0491.
[6] M. Dong, Y. Sun, D.J. Dunstan, R.J. Young, D.G. Papageorgiou, Nanoscale 16 (2024) 13247.
[7] J. Yoon, S. Kim, K.H. Park, S. Lee, S.J. Kim, H. Lee, T. Oh, C.M. Koo, Small Methods 7 (2023) 2201579.
[8] F.E.A. Latif, M. Khalid, A. Numan, N.A. Manaf, N.M. Mubarak, H.A. Zaharin, E. C. Abdullah, J. Mol. Struct. 1329 (2025) 141407.
[9] Y. Zhang, Z. Ma, K. Ruan, J. Gu, Adv. Photonics Res. 4 (2022) 2300224.
[10] L. Guo, K. Hu, H. Wang, Polymers 15 (2023) 2352.
[11] Q. Gao, M. Feng, E. Li, C. Liu, C. Shen, X. Liu, Macromol. Mater. Eng. 305 (2020) 2000343.
[12] M. Licciardello, C. Traldi, M. Bortolameazzi, D. Testore, G. Ciardelli, C. Tonda-Turo, Front. Biomater. Sci. 3 (2024) 1362599.
[13] A. Shaker, A.T. Khedewy, M.A. Hassan, M.A.A. El-Baky, Sci. Rep. 13 (2023) 17368.
[14] N.Z. Renkler, Z.U.D. Babar, M. Barra, I. Cruz-Maya, R. De Santis, R.d. Girolamo, M. Marelli, A.M. Ferretti, A. Zaheer, V. Iannotti, V. Guarino, Macromol. Mater. Eng. 310 (2025) 2400433.
[15] X. Li, S. Wang, M. Zheng, Z. Ma, Y. Chen, L. Deng, W. Xu, G. Fan, S. Khademolqorani, S.N. Banitaba, A.I. Osman, Nanoscale Horiz. 9 (2024) 1703.
[16] C. Liang, Z. Fan, Y. Zhu, Y. Cao, J. Kang, J. Tao, Front. Chem. 12 (2024) 1471148.
[17] T. Li, L. Yao, Q. Liu, J. Gu, R. Luo, J. Li, X. Yan, W. Wang, P. Liu, B. Chen, W. Zhang, W. Abbas, R. Naz, D. Zhang, Angew. Chem. Int. Ed. 57 (2018) 6115.
[18] B. Isaac, R.M. Taylor, K. Reifsnider, Fibers 9 (2021) 4.
[19] J. Huang, Z. Li, F. Liu, W. Wei, X. Xu, Z. Liu, J. Appl. Polym. Sci. 140 (2023) e54582.
[20] T.-L. Ma, S.-C. Yang, T. Cheng, M.-Y. Chen, J.-H. Wu, S.-L. Liao, W.-L. Chen, W.-F. Su, J. Mater. Chem. B 10 (2022) 6372.
[21] Z. Yuan, S. Ju, W. Li, H. Guo, K. Chen, M. Yue, X. Yu, Y. Wang, Chem. Eng. J. 450 (2022) 138453.
[22] J. FitzPatrick, Y. Gogotsi, MRS Bull. 50 (2025) 1351.
[23] D. Parajuli, N. Murali, D.K. C, B. Karki, K. Samatha, A.A. Kim, M. Park, B. Pant, Polymers 14 (2022) 3433.
[24] B. Pant, M. Park, A.A. Kim, Micromachines 14 (2023) 1477.
[25] H. Zhou, F. Wang, Y. Wang, C. Li, C. Shi, Y. Liu, Z. Ling, RSC Adv. 11 (2021) 5512.
[26] M. Malaki, R.S. Varma, Nanomicro Lett. 15 (2023) 116.
[27] M. Maleki, A. Natalello, R. Pugliese, F. Gelain, Acta Biomater. 51 (2017) 268.
[28] C.-Y. Lin, S.-C. Luo, J.-S. Yu, T.-C. Chen, W.-F. Su, A.C.S. Appl, Bio Mater. 2 (2019) 518.
[29] R.S. Azam, D.A. Almasri, R. Alfahel, A.H. Hawari, M.K. Hassan, A.A. Elzatahry, K. A. Mahmoud, Membranes 12 (2022) 406.
[30] Q. Zeng, R. Wang, Z. Li, J. Lin, L. Guo, Y. Zhang, Z. Peng, A.C.S. Appl, Mater. Interfaces 18 (8) (2026) 13086.
[31] C. Likitaporn, M. Okhawilai, P. Kasemsiri, J. Qin, P. Potiyaraj, H. Uyama, Sci. Rep. 12 (2022) 19915.
[32] M.R. Maurya, M.S. Sha, L. Latrous, A. Megriche, K.K. Sadasivuni, J. Polym. Res. 31 (2024) 345.
[33] A. Prasad, J. Hasse, T. Steimle, D. Nepal, G.J. Frank, V. Varshney, Compos. Part B Eng. 284 (2024) 111689.
[34] Z. Ling, C.E. Ren, M.-Q. Zhao, J. Yang, J.M. Giammarco, J. Qiu, M.W. Barsoum, Y. Gogotsi, PNAS 111 (47) (2014) 16676.
[35] S. Metwally, U. Stachewicz, Mater. Sci. Eng. C 104 (2019) 109883.